

Validation and traceability of multi-parameter miniaturized radiosondes for environmental observations

Shahbozbek Abdunabiev^{a,b}, Andrea Merlone^c, Chiara Musacchio^c, Miryam Paredes^a, Eros Pasero^b, Daniela Tordella^a

^a*Dipartimento di Scienza Applicata e Tecnologia, Politecnico di Torino, 10129 Torino, Italy*

^b*Dipartimento di Elettronica e Telecomunicazioni, Politecnico di Torino, 10129 Torino, Italy*

^c*Istituto Nazionale di Ricerca Metrologica, 10135 Torino, Italy*

Abstract

The aim of the work is to design and develop light (less than 20 gr), expendable radioprobes to study complex micro-physical and chemical processes inside warm clouds. This includes the tracking of turbulent, both saturated and unsaturated, air parcels. With this new kind of radiosonde, we thus aim to obtain Lagrangian statistics of the intense turbulence inside warm clouds and of the lower intensity turbulence typical of the air surrounding them. The radiosonde is made of the radioprobe (the electronic board) attached to a biodegradable balloon filled with a mixture of helium and air. The system is able to float inside/into clouds for a time span of the order of a few hours and measure fluctuations of air temperature, pressure, humidity position, velocity and acceleration along with its own trajectory which

Preliminary in-field experiments were carried out with a single and multiple radiosondes in different environments. Sensor readings are validated by comparison with reference values provided by INRIM traceable instrumentation and/or ARPA (Piemonte) and OAVdA nearby meteorological stations. The last two experiments, INRIM, September 29, 2021 and OAVdA, February 10, 2022, addressed the possibility to implement a distance neighbor graph algorithm (Richardson LF - 1926) conceived for turbulent dispersion analysis in the atmosphere and which, actually, has not been yet realized in the context of in-field atmospheric observations.

Keywords: Cloud, Lagrangian tracking, Radiosonde, Dispersion, Diffusion, Sensor fusion, Stereo vision

1. Introduction

Clouds are the largest source of uncertainty in weather prediction and climate science. They are remaining as a weak link in modeling of the atmospheric circulation. This is rooted in the fact that clouds depend on the physical and chemical processes over a huge range of scales, from the collisions of micron-sized droplets and particles to the airflow dynamics on the scales of thousands of meters (...). Since ambiguities exist related to representation of clouds in climate models, we need more observations.

However not all types of clouds are relevant, when we discuss important issues such as global warming. Due to reflectivity, clouds cool the earth by around 12 °C, an effect largely caused by *stratocumulus (warm)* clouds. However, at the same time, they heat the earth by around 7 °C by reflecting emitted radiation, an effect largely caused by cirrus clouds. This averages out to a net loss of 5 °C[1].

To understand why cloud evolves as observed, why heavy rainfalls can not be predicted precisely in sub-grid parametrization, one must know evolution of the internal fluctuations and and sources of fluctuations (forces) from direct measurements. In order to determine the fluctuations and forces relevant to cloud dynamics, we need to measure quantities such as temperature, pressure, moisture (humidity), accelerations, velocity fields inside clouds. This can be achieved from a collection of simultaneous point-to-point direct measurements in different parts of the cloud to obtain precise point measurements and retrieve (generate) information about general view of the the cloud flow. And these kind of observations are not directly available with current instrumentation and measurement techniques.

Remote sensing platforms, either ground based (...), airborne (...), or spaceborne (...), are not particularly useful owing to the relatively long times required to complete a scan and the inability to penetrate clouds and precipitation[2]. Nowadays radars are the main source of observation information of clouds. They can provide the exact information about the morphology of clouds, precipitation levels, liquid water content. Dual-Doppler observations can also provide information on velocity, rotation, thus so vorticity field.

Direct numerical simulations can also provide insights for understanding internal fluctuations and intermittency of clouds. However, only using them

can not provide us full picture. Since, numerical simulations can resolve only small portion of clouds (1-10 meters, (...)). And it is also computationally expensive to resolve all physical and chemical processes inside clouds for the large portion of the cloud (1-10 km, (...)).

It is important to study small-scale fluctuations inside clouds and their counterparts (clear-air) within the sub-grid scale (usually grid size is 10 km, but state-of-the art is 2 km with ~ 90 million core hours [3, 4]) of the existing climate simulations. This is because convective parameterization schemes in global climate model (GCM) simulations may be underestimated (overestimated), [5]. That is why we need more realistic numerical simulations and in-field experiments: i) Numerical simulations that can resolve small-scale dynamics of the clouds and their interaction with surrounding clear-air; ii) In-field experiments that can provide small-scale variations of the physical quantities (velocity, acceleration, pressure, humidity, temperature, etc.) from direct measurements.

There are two different approaches in climate simulation models for representing clouds and cloudiness: **convection-parameterizing** and **convection-resolving**. The convection-parameterizing simulations overestimates the humidity (cloudiness) in low-level (close to the ground, 2m above the ground, 850 hPa) and underestimates the humidity in mid-level (700 hPa, 500 hPa). In the upper-level (200 hPa) simulations, usually the both simulation models act in the same way. High level of cloudiness in mid-level altitudes are due to strong and frequent updrafts, strong vertical mixing and favorable dynamical and microphysical conditions for the formation of the mixed-phase clouds.[4]

This paper is about a notable gap in ability to *directly* observe *fluctuations* of physical and chemical quantities inside mid-level (*warm*) clouds.

To study turbulent characteristics (intermittency, high-energy level in different parts of the cloud) of the clouds by means of numerical simulations (...) and in-field measurements (...) were important topics for the research community.

In summary, we need new instrumentation and/or measurement techniques to provide reliable, real-time in-filed observations inside clouds. It is difficult to find the similar in-field experiments in the current application context. But, we can find some similar instrumentation setups, such as Swenson et al. [6], some other (...), etc. The advantage of such in-field measurement system is threefold: (i) Direct quantification of Lagrangian turbulent dispersion and diffusion from real, in-field measurement; (ii) Tracking small variations of physical quantities inside real clouds; (iii) General under-

standing of the cloud dynamics with simultaneous measurements in different parts of the cloud.

For this reason the COMPLETE project was submitted to H2020. The project was inspired by the experimental method introduced by Richardson L. F. (1926) [7]. And this in-field experiment was not carried out since then. The project is an interdisciplinary and aimed to decrease knowledge gaps in understanding cloud dynamics by combining skills from different areas. Within project it is proposed to use the numerical simulations, laboratory and in-field experiments.

And here, we are presenting our work on in-field measurements. For the in-field measurements, mini, biodegradable radiosondes are designed and developed. Mini radiosonde is only 5x5 cm and weights 7 grams without battery with helium balloon, which has radius of 20 cm (much less than traditional weather balloons). Recently, the second version of the mini radiosonde has been developed, which has dimension of 3.5x4 cm and weights around 3 grams only. Thus, for the future experiments smaller balloons can be used. Each radiosonde include various set of sensors, such as pressure, humidity, temperature, IMU (Intertial Measurement Unit) and GNSS sensors. With the help of radiosondes we aim to create a new Lagrangian based, cloud fluctuation datasets. The generated dataset is required to reduce the fragmentation of results and knowledge in this field. By providing more accurate data obtained by radiosondes, we try to reduce ambiguities and limitations of numerical simulation and modeling.

In the Lagrangian reference system, the fluid flow properties are determined by tracking the motion and properties of the individual fluid particles as they move in time. For example, the temperature will be measured along the trajectory of the fluid particle as time passes. In this way, if we can track many fluid particles, we can have an idea about fluid properties for the whole domain (...).

Usually sensors introduce high and low frequency faults. High frequency faults may arise when the GNSS signals undergo multi-path errors. These errors occur when the GNSS signal is reflected off one or more surfaces before it reaches the receiver antenna. Low frequency faults can be introduced by IMU sensor readings [8]. It is called sensor bias, offset of measurement while sensor is not measuring anything. This bias offset can be removed by calibrating the IMU sensor output. The removal of bias in the sensors does not however provide perfect solutions because of white noise introduced by sensors. Further application of subsequent filters (e.g. Kalman) help us to

remove effects of errors in our measurements.

In the Section 2 we describe the measurement system. Then, in Section 3, we discuss the traceability of the system, quality of the obtained dataset and validation with reference systems. In Section 4, we provide the results from the preliminary in-field experiment campaigns and we conclude our discussion with Section 5.

2. Measurement system description

Getting the probes to observe relevant parts of the cloud over different range of scales during cloud lifetime is challenging in terms of instrumentation setup. To accomplish this challenging task, the following measurement system was suggested for in-field experiments, see Figure 1. The measurement system consists of the following building blocks: a set of radiosondes, ground stations and post-processing machine. We aim to put a set of radiosondes inside warm clouds (or any other atmospheric environment), where each radiosonde can passively follow the fluid flow. Thus, it can be possible to have an idea about real dynamics of the surrounding fluid, which is cloud, when balloon is inside it, or clear air when it is outside.

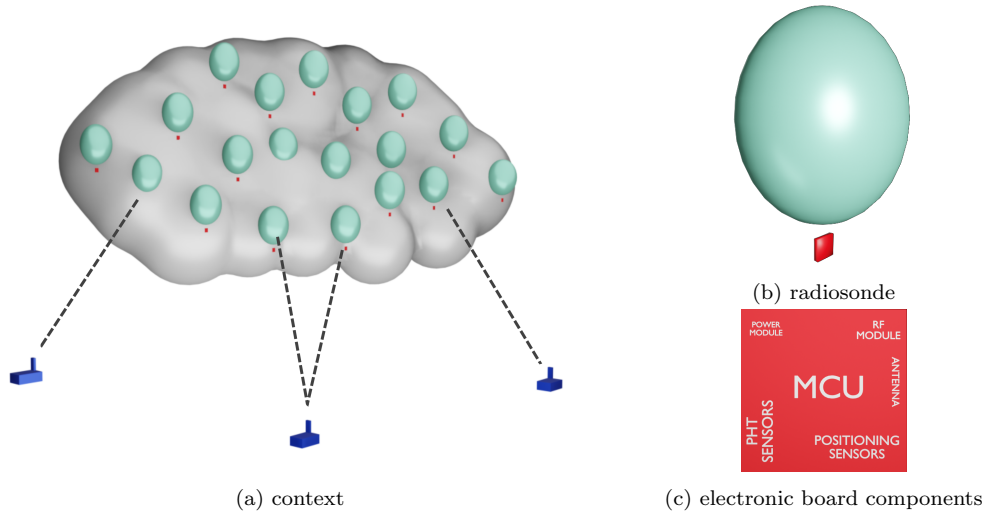


Figure 1: In-field measurement measurement context.

Each radiosonde transmits sensor readings to ground stations with Lora radio transmission protocol. LoRa is a relatively new proprietary communication technology that allows long-range communication distances while

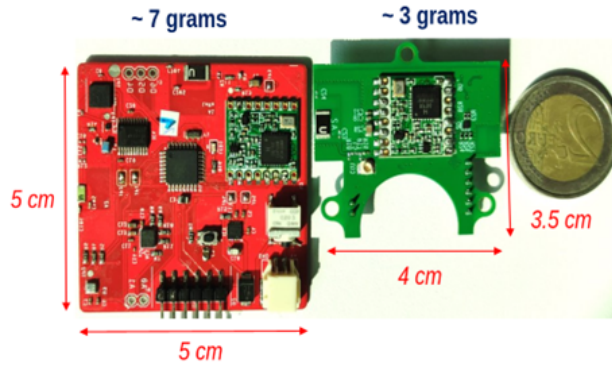


Figure 2: Current (red) and 2nd (green) prototype of the radiosonde board.

consuming very little power. It utilizes license-free Industrial, Scientific and Medical ISM frequency bands to exchange information at low data rates. Ground stations receive data from radiosondes, they are connected to post-processing machine. We store all data in post-processing machine. In order to reduce data losses same data transmitted by radiosonde can be received by different ground stations.

The design of the radiosonde electronic board, tests inside environmental chamber and initial the performance evolution of the radiosonde in field experiments were described in the previous work by Miryam et. al[9].

In Figure 1(b) we can see the radiosonde design: it includes biodegradable balloon and radioprobe (electronic board). The balloon is filled with helium and radioprobe is connected to the battery. They are attached together and can float (stay on air) for multiple hours. Embedded electronics (microprocessor, radio module and sensors) can measure velocity, acceleration, pressure, temperature and humidity fluctuations in the surrounding environment. This configuration is selected as a result of the in-field experiment tests (see Sections 3 and 4 for discussion).

2.1. Radioprobe

Furthermore, Figure 2 shows the current (red) and newly optimized (green) prototypes of the radioprobe. Nowadays, the new version of the radioprobe prototype is under hardware and software tests. Thus, the focus of the discussion will be current working prototype. The building blocks of the radioprobe board are illustrated in the Figure 1(c), which consists of microcontroller, power module, radio transmission module, sensors and antennas. The *micro-*

controller is data-processing and control unit, which allows to control other units, acquire sensor readings and execute function calls in an automated way inside the device. The *radio transmission module* of the radioprobe enables the one-way wireless communication with ground stations using radio frequency signals. *PHT* (Pressure, Humidity, Temperature), *IMU* (Inertial Measurement Unit) and *GNSS* (Global Navigation Satellite System) *sensors* provide sensor readings of physical quantities [9]. Those quantities together with sensor operating ranges, sample rate and provider functional unit are described in Table 1. Sensors are chosen based on their compact size and

Table 1: Sensor operating ranges.

Physical quantity	Range	Sample time	Device
Pressure	[300, 1100] mbar	4 s	PHT
Humidity	[0, 100] %	4 s	PHT
Temperature	[-40, 85] °C	4 s	PHT
Longitude	degrees	4 s	GNSS
Latitude	degrees	4 s	GNSS
Altitude	m	4 s	GNSS
Acceleration	[-16, 16] g	4 s	IMU
Course	[-1, 1] quats	4 s	IMU

low-power consumption. Furthermore, they are configured to work in energy-efficient modes. For example, GNSS by U-blox has compact size and can be configured to operate in e-mode. In other studies, researchers exploited high precision GNSS sensors [6], (...), however such sensors consume more power, which is crucial for our application context. Moreover, GNSS sensor provides compact PVT (Position, Velocity and Time) navigation information by using proprietary protocol [10], which can not provided in a single sensor reading by using traditional NMEA protocol[11].

2.2. Biodegradable balloon and stable floating

The radiosonde system should float at an almost constant altitude during the experiments. To float at a fixed altitude, the balloon volume must remain relatively the same during flight [12, 13]. Therefore, the balloons used in our experiments were made from non-elastic materials. Furthermore, to minimize environmental impact of the radiosonde system, the used electronic components and balloon material should be as biodegradable as

possible. The material characteristics of the balloon, processing methods, and polymer coatings were studied in the COMPLETE project by Basso et al. [12].

They studied green polymers, such as Mater Bi and PLA were studied and compared with materials used for traditional weather balloon production, such as Latex and Mylar. The properties of the above-mentioned materials were examined in laboratory experiments in collaboration with IIT Genoa. The main properties of interest are the *tensile strength*, *hydrophobicity*, *helium permeability*, and *resistance to variations* of the surrounding temperature and humidity. As a result of experiments, it can be concluded that Mater-Bi with applied coatings was the best fit for satisfying above properties[12].

For the recent in-field experiments spherical balloons ($R = 20$ cm) were made from store bought Mater-Bi bags. Selected Mater-Bi material has $20 \mu\text{m}$ thickness a density of 1.24 g cm^{-3} , which is thinner than the previous studies ($30 \mu\text{m}$) carried out by Basso et al.[12]. Thus, the balloon mass was reduced by a factor of 1.5, which in turn reduced the overall payload budget(eq. 1). Balloon dimensions were identified based on the weight of the radiosonde electronic board with battery and atmospheric parameters in a target floating altitude (see Table 2). The volume of the balloon should satisfy the following equation for stable floating in a fixed altitude:

$$V_b = \frac{m_{total}}{\rho_a(1 - M_g/M_a)} = \frac{m_r + m_b}{\rho_a(1 - M_g/M_a)}, \quad (1)$$

where m_r is mass of the radioprobe with battery and connections, m_b is the mass of the balloon, ρ_a is air density in a given altitude, M_a and M_g are molar masses of air and gas inside balloon. $m_b = S\Delta d\rho_m = 4\pi R^2 \Delta d \rho_m$, where S is surface area of the spherical balloon with radius R . Δd and ρ_m are thickness and density of the Mater-Bi material.

Figure 3 shows the relationship between total liftable payload (excluding balloon weight, m_b) and floating altitude for the fixed balloon dimensions. In the current design, weight of the radioprobe with battery and connections, m_r , is 17.5 grams (see Table 3 for details). It can be lifted up to 1725 meters above sea level with 20 cm radius balloon; up to 2650 meters with 21 cm radius balloon and so on. While, the second version of the prototype (8.5 grams) allows us to use even smaller balloons and less amount of gas (e.g. Helium) to reach the same floating altitude.

Table 2: Standard atmospheric parameters for possible operating altitude range of the radiosonde. Here, altitude is given as height above sea level, T is temperature, P is the pressure and ρ_a is air density.

Altitude [m]	T [K]	P [hPa]	ρ_a [kg/m^3]
0	288	1013	1.22
500	285	950	1.17
1000	282	900	1.11
1500	278	850	1.06
2000	275	795	1.01
2500	272	748	0.95
3000	269	701	0.90

Table 3: Radiosonde payload weight.

Part	Mass [grams]	
	Current design	New design
Radioprobe	7	3
Battery	8	3
Connections	2.5	2.5
Balloon	12.5 (R=20 cm)	9 (R=17 cm)
Total	30	17.5

2.3. Ground station and network architecture

LoRa based wireless sensor network (WSN) concept was adopted for the radiosonde network. The star architecture was used, where each radiosonde is connected to the ground receiver station with point-to-point link. The feasibility analysis of the selected network architecture was carried out in different application scenarios [14, 15, 16]. First in-field test of the network architecture in the current application context were presented here [9]. In most cases, LoRa protocol based WSN networks are used as within LoRaWAN network. However, in this work, LoRa protocol is used to create an ad hoc private network and adapt the technology to the working scenario[9]. Therefore, the commercial off-the-shelf LoRa-based transceiver module RFM95 from HopeRF was used. It is a module featuring long-range spread spectrum communication links and high immunity to interference whilst optimizing the power use [9]. This module allows power-transmission ranges within 5 dBm (3.16 mW) to 20 dBm (100 mW), although according to the regulations re-

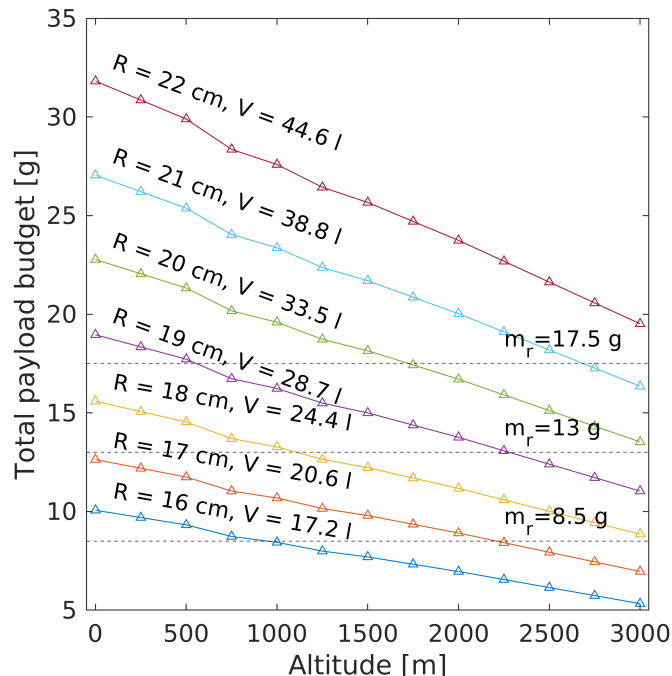


Figure 3: Total payload budget with respect to the operating altitude. Each line represents variation of the payload budget along altitude for a given balloon dimensions: R is the radius of the spherical balloon and V is the volume in liters. As it can be seen from the Table 2, the air density changes with the altitude, thus the lifting force. Horizontal lines shows weight of the the radioisotope: current version (17.5 g), the second optimized version (8.5 g) and medium (13 g). This weight includes battery and all equipment needed to attach the radioisotope to the balloon. Detailed breakdown of the radioisotope weight is given in the Table 3.

leased by the European Telecommunications Standards Institute (ETSI), the maximum power allowed in the European area is 14 dBm (25.12 mW) [17].

2.4. Data acquisition and processing

Data-processing flow of the radioprobe can be seen in Figure 4. The flow consists of steps to be performed by radioprobe (transmitter) and ground station (receiver). Some of the processing will be done directly in the transmitter side, and more power and time consuming part will be done in the receiver side with the help of the post-processing machine.

As it can be observed from the Figure 4, sensor data is processed by

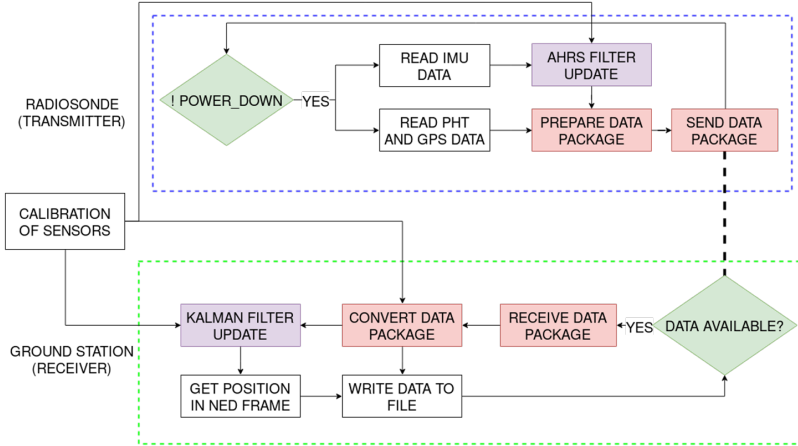


Figure 4: Radiosonde system processing flow.

AHRS (Attitude and Heading Reference System) filter before sending to the ground station. The AHRS filter acquires readings from 9-DOF IMU sensor (3x accelerometer, 3x gyroscope and 3x magnetometer) and provides course (orientation) of the radioprobe as output. In order to remove possible errors introduced by sensor readings, the AHRS filter also uses sensor calibration data [18]. IMU sensor readings are provided with respect to the body frame (xyz) of the radioprobe. Those readings can be translated into local experiment frame ($X_e Y_e Z_e$) by using orientation data from AHRS filter.

Furthermore, acceleration data represented in local experiment frame can be handful to obtain positioning information during GNSS outages. Acceleration data are fused with GNSS sensor data by means of Kalman Filter. It has two different operating modes: *predict* and *update* [19]. In predict mode, we use IMU data to provide position information with respect to the last reference position. As soon as GNSS data is available, we update the reference position. In this way, we can have position information during GNSS outages. Since the GNSS sensor consumes relatively more power than IMU and other sensors, this approach helps us to reduce power consumption.

3. Results and discussion

As it is stated in the previous sections, the preliminary results were presented in the previous works by Basso et al.[12] and Miryam et al.[9]. However, in the previous works, not all parts of the measurement system

were tested and validated with extensive in-field campaigns. Furthermore, it is possible to apply a certain post-processing algorithms only when proper in-field experiments are carried out. In the following subsections, recently obtained results are described as a set of reached milestones.

The measurement system was compared and validated with respect to traditional instrumentation. Type of experiments can be carried out with proposed measurement system are: (i) fixed point measurements at ground level; (ii) vertical profiling measurements of atmosphere; (iii) Lagrangian tracking measurements with a cluster of radiosondes.

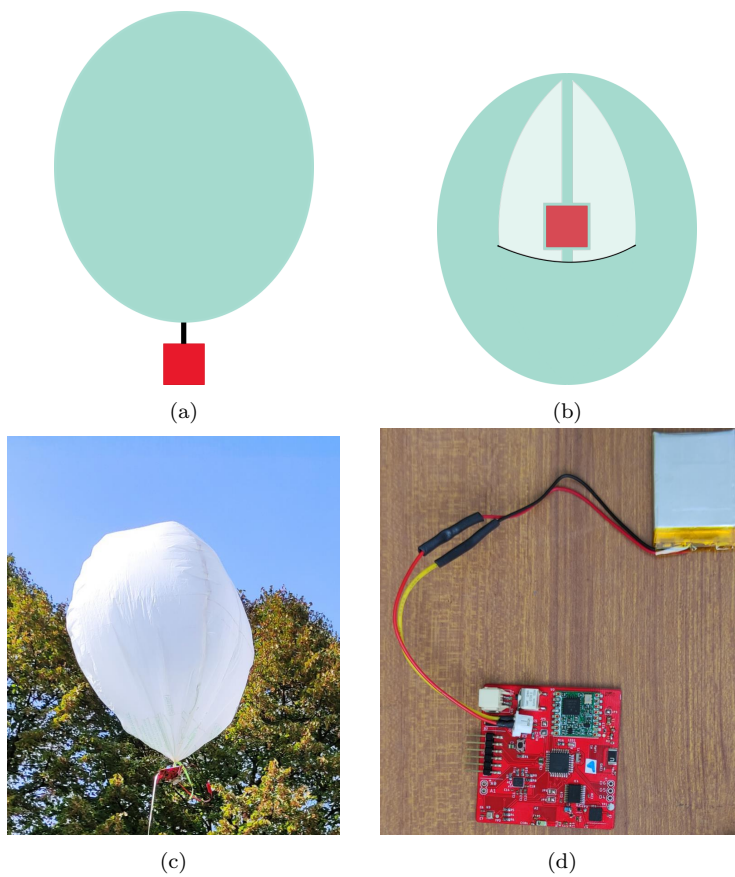


Figure 5: Two different configurations for radiosonde. (a) configuration A: radioprobe board is **outside** the balloon. (b) configuration B: radioprobe board is in the pocket **inside** the balloon. (c) radiosonde in configuration A, attached to the ground with a thread. (d) radioprobe board with battery.

3.1. Pre-launch calibration and fixed point measurements

In-field test started with testing various configurations for the radioprobe and validating sensor measurements with respect to fixed point measurements at ground level. Figure 5 illustrates two different configurations, that are tested and validated with respect to reference station at campus of INRIM.

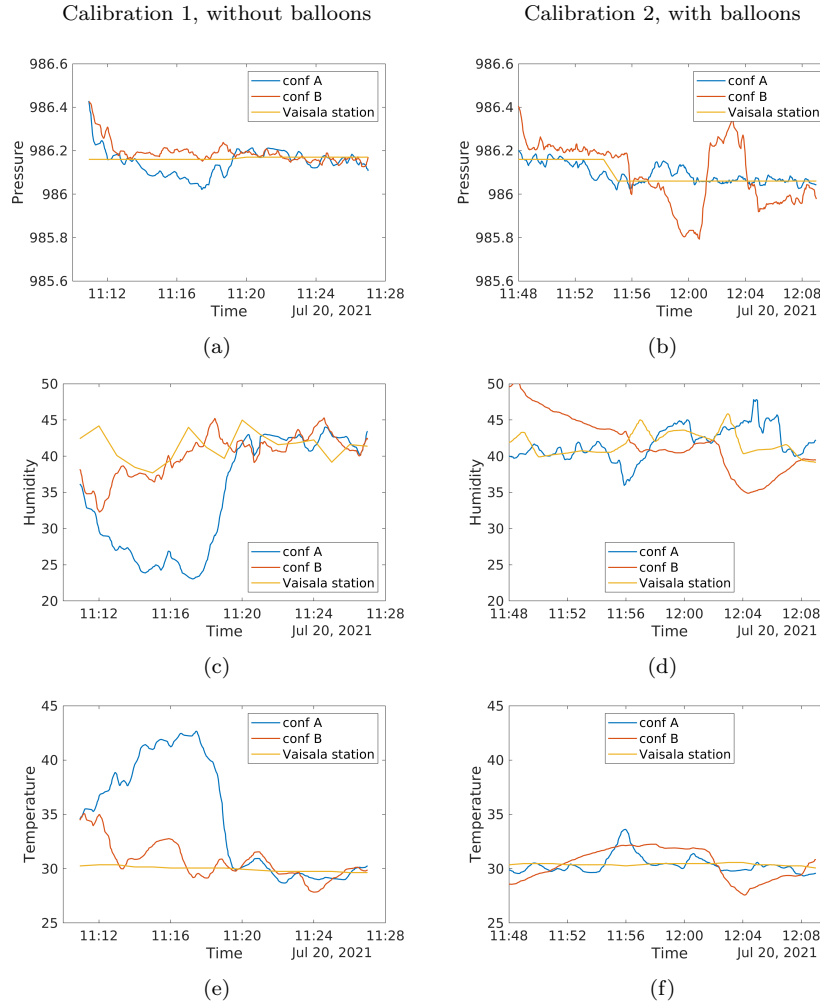


Figure 6: Pressure, humidity and temperature readings from radiosondes with two different configurations. (a,c,e) First sensor readings without balloons. (b,d,f) Sensor readings after attaching the balloons. conf A: radioprobe is **outside** the balloon. conf B: radioprobe is **inside** the balloon.

Both configurations were tested before and after attaching the balloons.

The second configuration (*conf. B*: radioprobe inside balloon) can introduce unintended biases into sensor readings. In Figure 6 we compared pressure, humidity and temperature readings from two configurations. Sensor readings are also compared with the fixed Vaisala station, which includes RS41 probe. The reference Viasala station was pre-calibrated and provides temperature, pressure and humidity sensor readings for all day long with 1 minute time interval.

In the first period of the experiment (Panels a,c,e), it can be seen that sensors take some period (~ 10 minutes, from 11.10 to 11.20) to warm up and catch up with Vaisala station readings. This is common behavior of MEMS sensors, particularly for atmospheric measurement sensors.((...)). After attaching radioprobes to the balloons, readings from configuration B started to show mismatches with reference station (Panels b,d,f), while readings of configuration A were aligned better with reference station measurements, particularly for pressure and temperature. However, some small fluctuations in temperature and humidity readings with respect to the fixed station can be due to the positioning and movement of our probes around the station.

This experiment helped to validate the proper configuration of the radiosonde, quantify biases and warm-up time of sensors.

3.2. Vertical atmospheric profiling measurements

The second dual-sonde launch experiment was held in collaboration with the Regional Agency for the Protection of the Environment (ARPA) of Piedmont region, on June 9, 2021 at Levaldigi Airport, Cuneo, Italy. The experiment site was equipped with automatic sounding system, where ARPA-Piemonte launch a radiosonde twice a day for atmospheric profiling measurements. In the the first dual-sonde launch experiment, we observed interference problems of GNSS sensor[9]. In that time, the radioprobe board was attached directly to the case of the Vaisala RS-41 probe. To resolve this issue during the second launch, the radioprobe was attached to the reference Vaisala probe with 80 cm offset.

During the experiment, data transmission continued around 1 hour, until the radioprobe reached almost ~ 9 km altitude and **13 km in distance**. We received packets in each 3-4 seconds and relative performance on our target altitudes (2-3 km) are also promising. In Figure 7, we can see the number of packets received in each minute (panel a) and in a given altitude (panel b) during the first 25 minutes of the launch. The original idea is to reach 1 Hz transmission rate. However, with the current computational parameters of

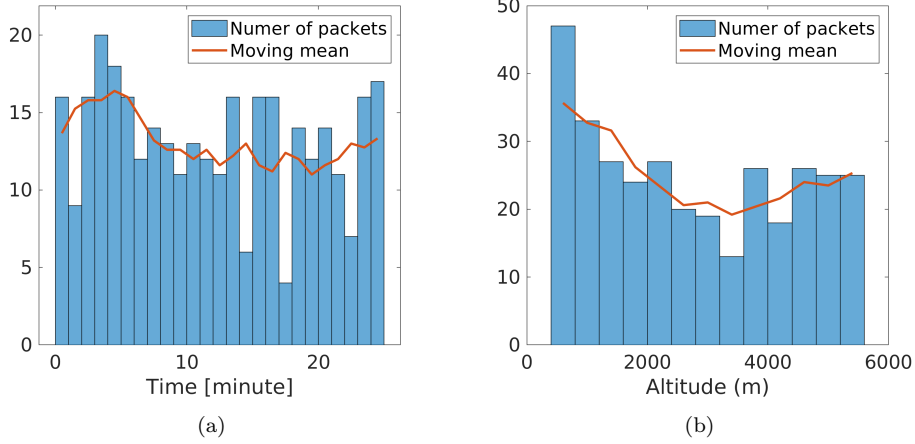


Figure 7: Packet transmission test for long distances in Levaldigi Airport with ARPA, Piedmont. (a) Number of packets received in each minute together with moving average. (b) Number of packets along altitude levels, bin size = 400 meters.

the radioprobe and data packet size, it is difficult to achieve. Moreover, the current prototype of the receiver station does not support multi-channel LoRa connections. It is agreed that the design of the new multi-channel receiver station can solve this issue. The new station, which is under development, can receive multiple connections in each channel as also used here[6]. In this way, the receiver station can receive simultaneously data packets from 10-20 radiosondes without packet losses due to collision.

Figure 8 shows the comparison of GNSS sensor measurements. It can be seen that raw GNSS readings of longitude, latitude and altitude already provide quite accurate results with respect to the reference system, prior to apply any filters.

GNSS sensor can also provide velocity readings in north, east and down directions, as it is plotted in Figure 9a. Horizontal wind speed was computed from north and east velocity components and was compared with horizontal wind speed readings of RS41 probe, see Fig. 9b. Wind speed was further analyzed with FFT (Fast Fourier Transform) to get preliminary results of power spectra of fluctuations. To compute the spectra, 30 minutes wind speed dataset was sampled with a 4s time step (see Fig. 9c), which gives frequency range from $5 \cdot 10^{-4} \text{s}^{-1}$ to 0.25s^{-1} and Nyquist frequency of 0.12s^{-1} ($2\pi/8 = \pi/4 \text{ rad/s}$), see Fig. 9d. The same kind of analysis can be performed with datasets of vertical velocity and temperature. The same

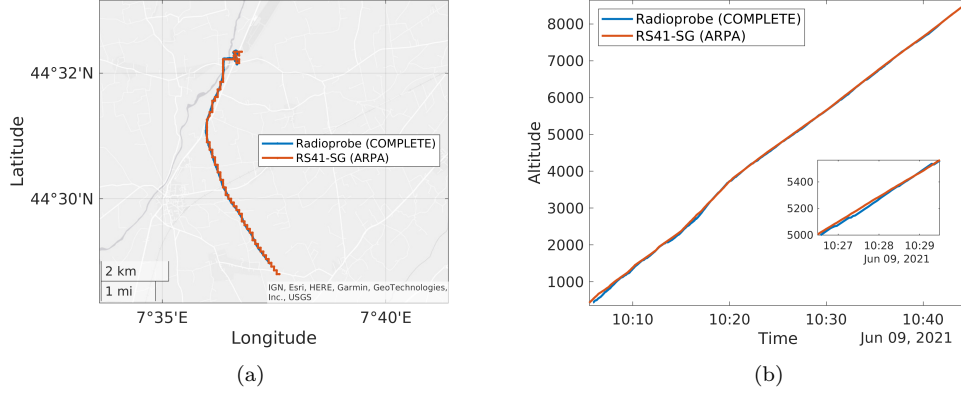


Figure 8: GNSS positioning measurements of the COMPLETE radioprobe and comparison with Vaisala RS-41 probe. (a) Map plot of longitude and latitude readings. (b) Altitude readings, the inset is plotted for better comparison.

power spectra analysis of the vertical velocity can be used to identify a cut off point of Brunt-Vaisala frequency, while vertical temperature profile (Fig. 10e) can be used to derive a complete profile of the Brunt-Vaisala frequency along the altitude[20, 21].

The plots in Figure 10 show that the radioprobe experienced some biases during the launch with respect to the Vaisala RS-41 probe. Biases are evident, especially for humidity and temperature readings, which is mainly due to heating and radiation in sunny day. However, it is unlikely that the biases inside clouds due to heating is noticeable. Furthermore, the sensor datasheet suggests that the air-flow in direction to the vent-hole of the PHT sensor has to be engineered in a way that a sufficient air exchange inside to outside will be possible. This aspect was already considered during the PCB board design, tests in environmental chamber and in field experiments [9]. However, it is believed that the second board design will improve humidity measurements. Due to slow response time, it is also suggested to use low data rates for atmospheric observation applications. To observe effects on the response time of the device for humidity measurements, which is 1 second to reach 63% of the step change, an air-flow velocity of approximately 1 m/s is needed[22]. For this purpose, sensor's response to environmental changes was tested and validated inside Kambic KK190 CHLT climatic chamber, which is in the Applied Thermodynamics Laboratory of the Italian National Metrology Institute (INRiM)[9] It is worth to mention that the PHT sensor, like

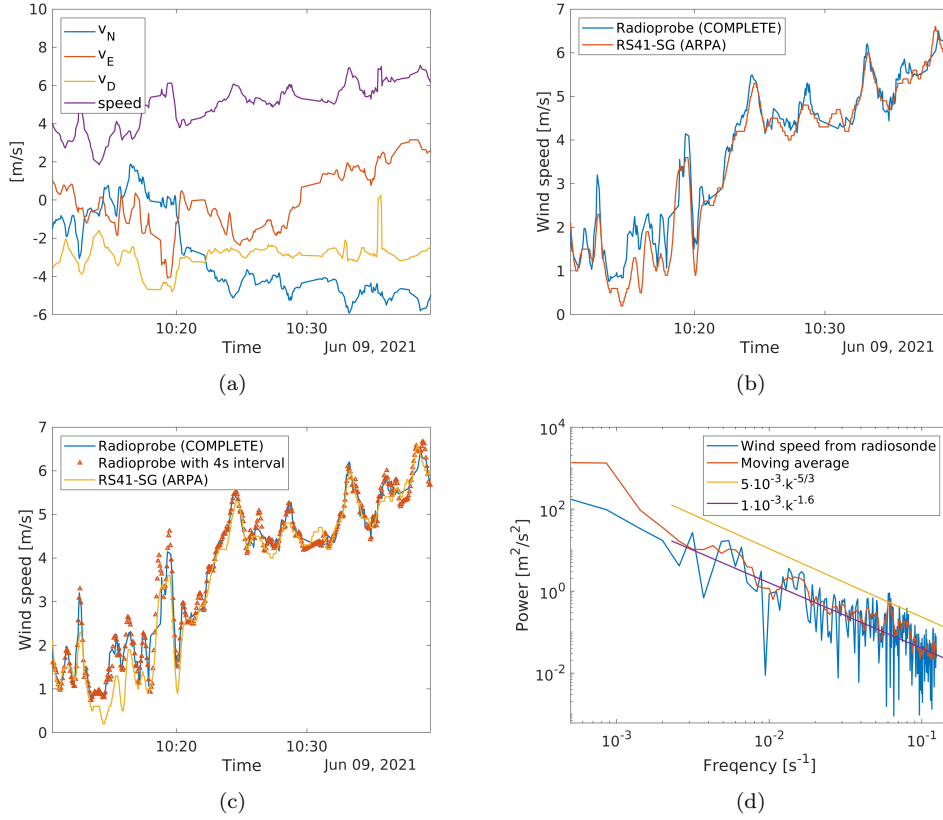


Figure 9: Velocity measurements of the radioprobe. (a) Velocity components and its magnitude. (b) Wind speed comparison from both radioprobes. For wind speed computation, only north and east components of velocity were used. (c) Wind speed from COMPLETE radioprobe: raw measurements (blue), resampled dataset with 4 second regular intervals (orange) and reference dataset from Vaisala probe. (d) Power spectrum of wind speed dataset of the COMPLETE radioprobe. Besides raw spectrum dataset (blue), moving average of the spectrum values (orange) and two trend lines (yellow and violet) are provided for comparison. Frequency range was taken based on Nyquist frequency, which is half of the sampling frequency, $f_s/2 = 0.125s^{-1}$.

other sensor components, was selected because of its compact size, low-power and low-cost characteristics.

4. In-field measurements with the cluster of radiosondes

In the previous section, tests and validation results were presented with respect to the traditional fixed and vertical profiling radiosondes. Here, we

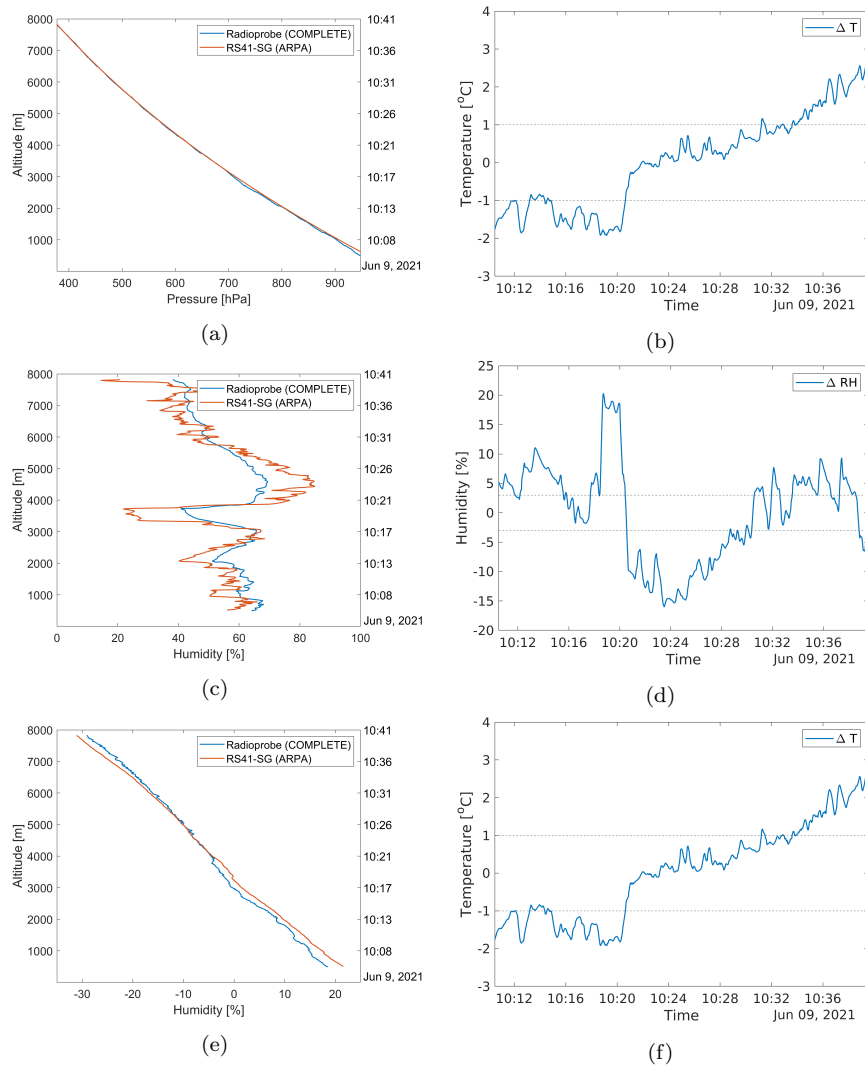


Figure 10: Pressure, humidity and temperature readings from radiosondes. (a, c, e) Comparison between COMPLETE and Vaisala probes. (b, d, f) Differences of two measurements. Dashed lines highlight absolute accuracy ranges of pressure (± 1 hPa), humidity ($\pm 3\%$) and temperature (± 1 °C)[22].

present preliminary results of simultaneous measurements from a cluster of radiosondes.

4.1. Multiple tethered radiosonde setup

Tests were started with experiments of 5 tethered radiosonde measurements as in Figure 11 at INRIM.



(a)



(b)

Figure 11: Experiment with multiple tethered radiosondes at INRIM. 5 radiosondes are prepared with 2 ground stations for this experiment. 2 radiosondes are highlighted with red and black colors for tracking them with video camera.

4.2. Validation of position with the stereo vision

The integration of gyroscope measurement errors will lead to an accumulating error in the calculated orientation. Therefore, gyroscopes alone cannot provide an absolute measurement of orientation. An accelerometer and magnetometer will measure the earth's gravitational and magnetic fields respectively and so provide an absolute reference of orientation. However, they are likely to be subject to high levels of noise; for example, accelerations due

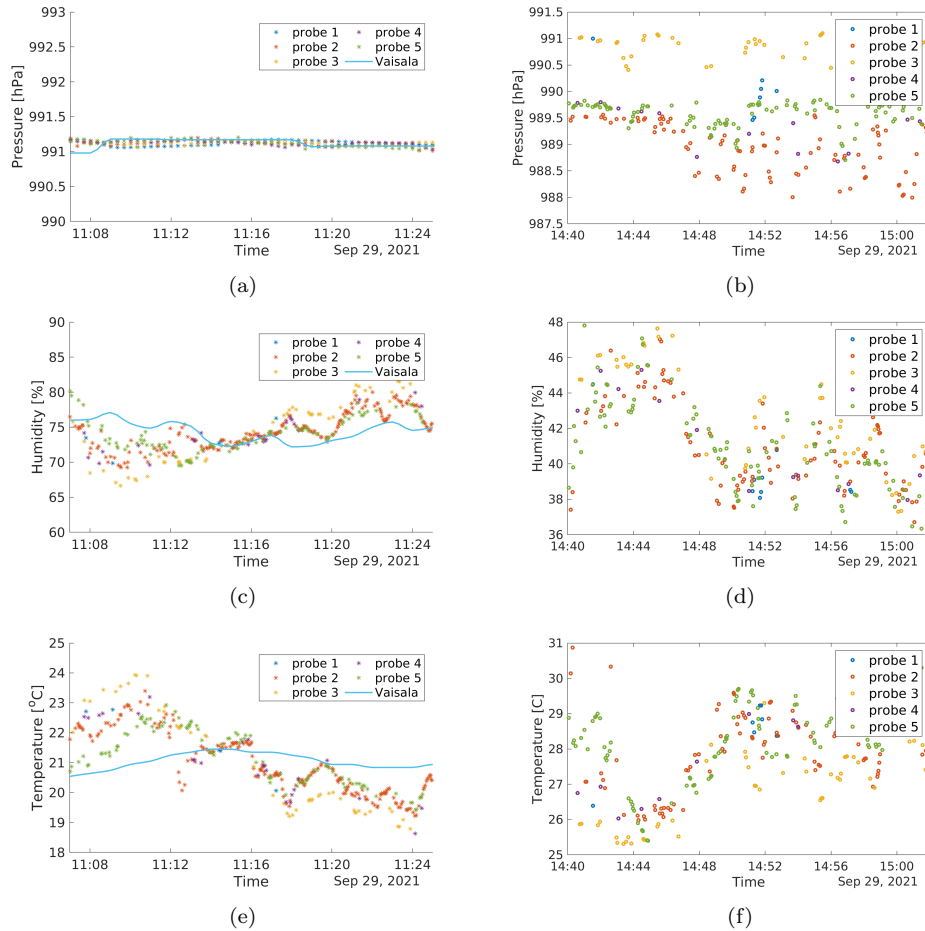


Figure 12: Pressure, humidity and temperature measurements in two phases of the experiment: calibration and fluctuating radiosondes, which are tethered to the ground. (a, c, e) PHT readings during calibration, where we removed systematic bias offsets. (b, d, f) Sensor readings during fluctuation phase of the radiosondes.

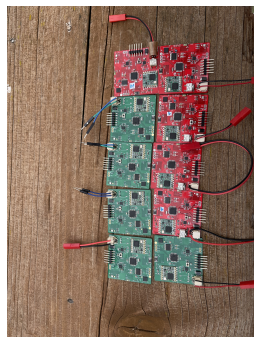
to motion will corrupt measured direction of gravity. The task of an orientation filter is to compute a single estimate of orientation through the optimal fusion of gyroscope, accelerometer and magnetometer measurements[18].

Innovative aspects of the AHRS filter by Madgwick et. al (2011)[18] include: a single adjustable parameter defined by observable systems characteristics; an analytically derived and optimized gradient descent algorithm enabling performance at low sampling rates; an on-line magnetic distortion

compensation algorithm; and gyroscope bias drift compensation. Recommended sampling rate is at least 20 Hz for Madgwick filter to work and provide proper output.

4.3. Free launch of radiosonde cluster

According to our knowledge, this experiment is one of the first observations done by using cluster of radiosondes to track fluctuations of quantities inside clouds and atmospheric flow field.



(a) radiosondes



(b) receiver station



(c) filling balloon with helium



(d) camera for stereo vision analysis



(e) calibration instrumentation



(f) PHT sensor calibration

Figure 13: Experiment setup with (a) 10 radiosondes, (b) 2 ground stations, (d) 2 cameras and (e) calibration instrumentation.

4.4. Relative positioning and dispersion analysis

It is expected that a combination of knowledge gained from the numerical simulations and in-field experiments will enable us to understand better the relative dispersion and diffusion in atmosphere.

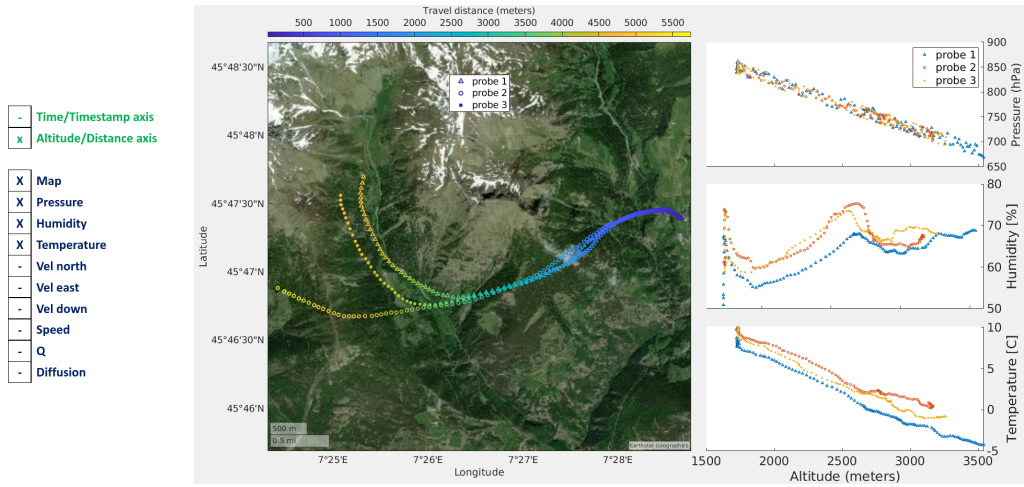


Figure 14: Position of the radioprobes together with corresponding pressure, humidity and temperature readings with respect to travel distance and altitude. Dashboard was generated with MATLAB.

Indeed simulation results provided preliminary insights for the setup of the in-field measurements, such as the selecting the initial launch point and initial neighborhood size.

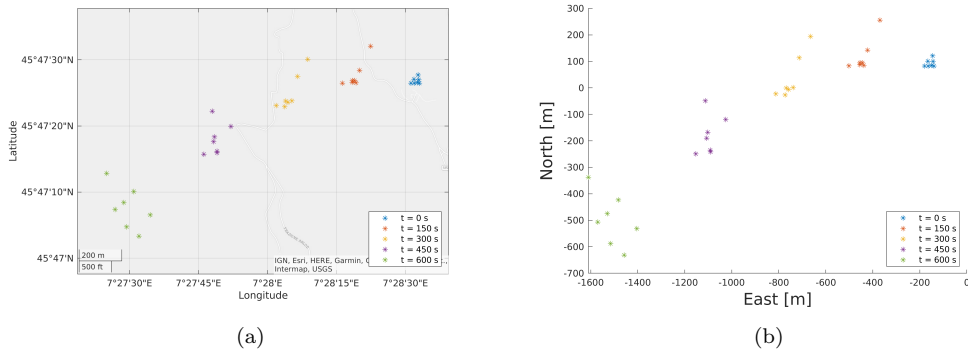


Figure 15: Relative positioning of the radiosondes are given in longitude-latitude frame (a) and north-east frame (b) with respect to experiment observation point (or initial launch point).

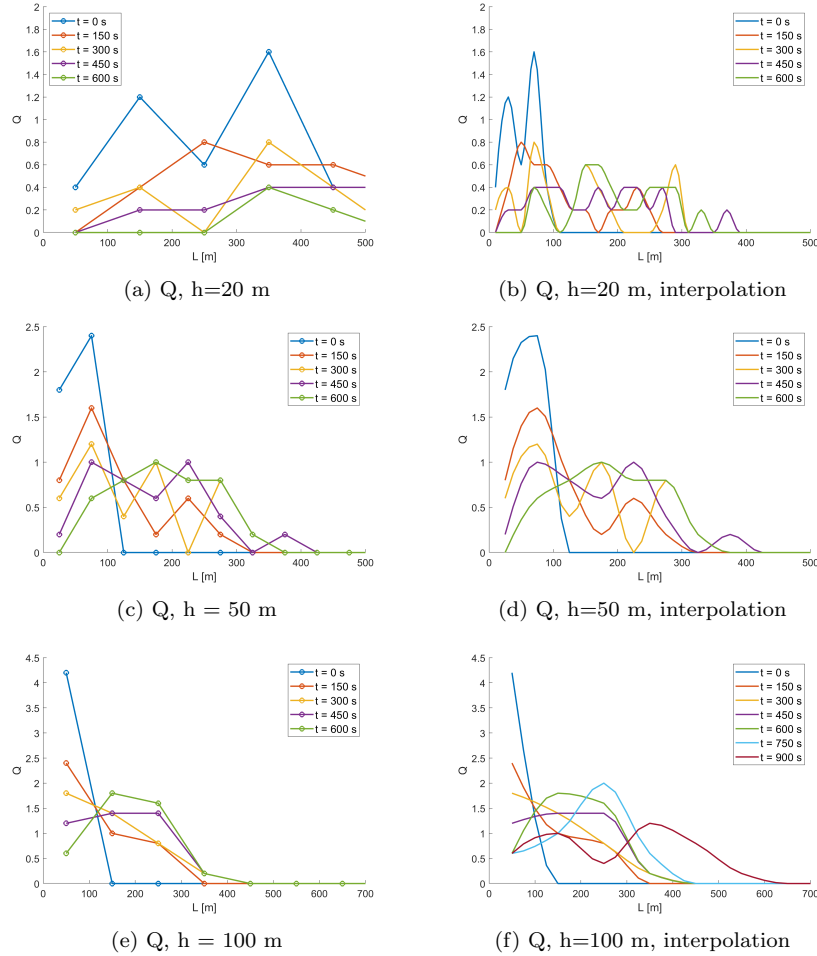


Figure 16: Distance-neighbor-graph is computed with different neighborhood size in the selected time instances. Initial time instance is 14:15:00. Following time instances are given in terms of seconds from initial time instance.

4.5. Basic spectral analysis from sensor readings

5. Conclusions

This work describes a new balloon-borne instrumentation system together with a consideration of the new measurement technique. In the paper, we highlighted all tests and in-field experiments, which helped us to validate and to bring the measurement system towards realization.

Currently, we are working on the optimization of the transmission and

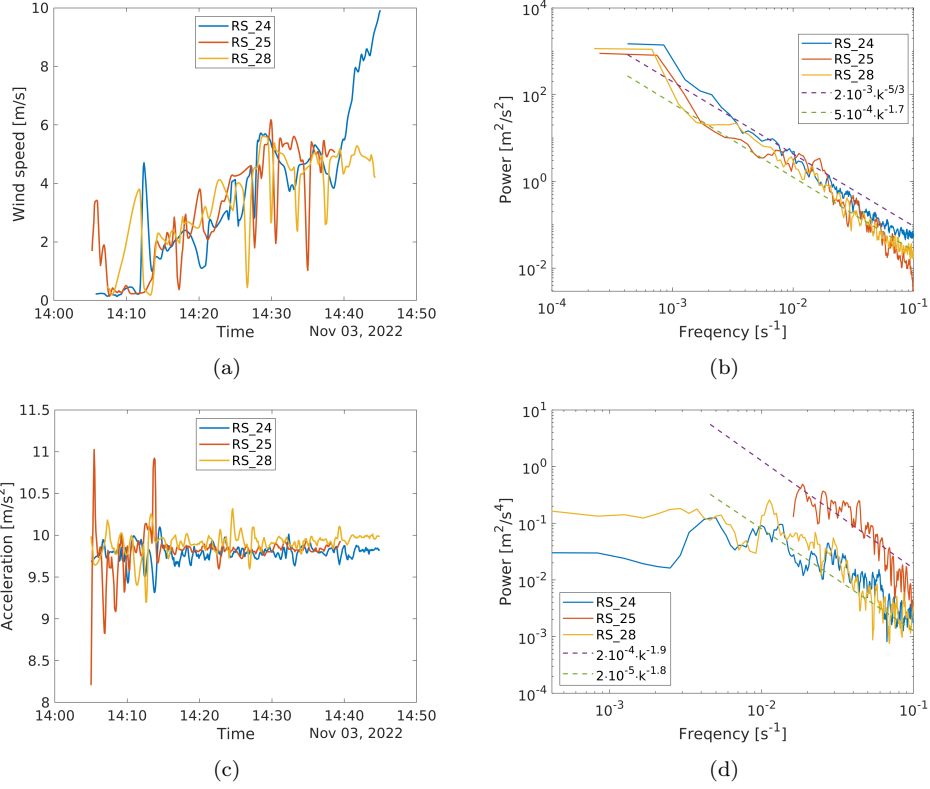


Figure 17: (a, c) Wind speed and magnitude of 3D acceleration measurements from 3 freely floating radioprobes. Dataset were resampled with 5 second regular intervals. (b, d) Power spectrum of wind speed and magnitude of 3D acceleration dataset of 3 radioprobes and two trend lines (violet and green) are provided for comparison. Frequency range is taken based on Nyquist frequency, $f_s/2$.

acquisition. The current data transmission rate is 1 packet per 3-4 seconds, which is acceptable for the current prototype. However, the prototype was already designed with optimized computational characteristics, weight and size. In the same time, new ground station is under development, which should allow users to receive data in higher rates and in parallel way. For this reason, we are developing custom gateway based on custom LoRa architecture.

By going forward, we would like to combine results coming from numerical simulations and in-field measurements, into a more comprehensive analysis of clouds, cloud microphysics, turbulent fluctuations.

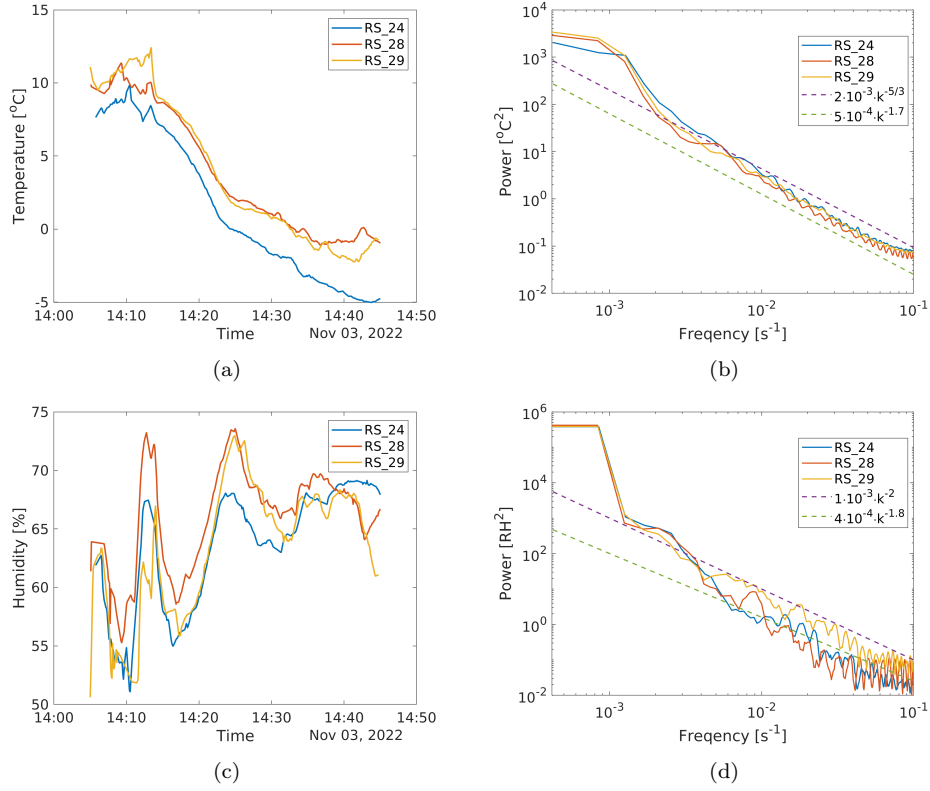


Figure 18: (a, c) Temperature and humidity measurements from 3 freely floating radio-probes. Dataset were resampled with 5 second regular intervals. (b) Power spectrum of temperature and humidity dataset of 3 radioprobes and two trend lines (violet and green) are provided for comparison. Frequency range is taken based on Nyquist frequency, $f_s/2$.

In the future radioprobe board sensors will be protected from radiation and precipitation sources with lightweight shield case.

Acknowledgments

This project has received funding from the Marie-Sklodowska Curie Actions (MSCA ITN ETN COMPLETE) under the European Union’s Horizon 2020 research and innovation program. Grant agreement 675675, *COMPLETE ITN-ETN NETWORK*. We would like to thank to *L’Osservatorio Astronomico della Regione Autonoma Valle d’Aosta*, Luca Tommassone and *ARPA, Piemonte* for hosting us during in-field experiment campaigns.

References

- [1] ISCCP, Cloud climatology. International Satellite Cloud Climatology Program, NASA, 2022. URL: <https://isccp.giss.nasa.gov/role.html>, [Online; accessed 18-March-2022].
- [2] P. M. Markowski, Y. P. Richardson, S. J. Richardson, A. Petersson, Aboveground thermodynamic observations in convective storms from balloonborne probes acting as pseudo-lagrangian drifters, *Bulletin of the American Meteorological Society* 99 (2018) 711 – 724. URL: <https://journals.ametsoc.org/view/journals/bams/99/4/bams-d-17-0204.1.xml>. <https://dx.doi.org/10.1175/BAMS-D-17-0204.1>.
- [3] PRACE, Climate simulations reach the next level of precision. Project access success stories, 2020. URL: <https://prace-ri.eu/climate-simulations-reach-the-next-level-of-precision/>, [Online; accessed 6-Dec-2022].
- [4] L. Hentgen, N. Ban, N. Kröner, D. Leutwyler, C. Schär, Clouds in convection-resolving climate simulations over europe, *Journal of Geophysical Research: Atmospheres* 124 (2019) 3849–3870. URL: <https://agupubs.onlinelibrary.wiley.com/doi/abs/10.1029/2018JD030150>. <https://dx.doi.org/https://doi.org/10.1029/2018JD030150>.
- [5] Z. Zhang, G. J. Zhang, Dependence of convective cloud properties and their transport on cloud fraction and gcm resolution diagnosed from a cloud-resolving model simulation, *Journal of Marine Science and Engineering* 10 (2022). URL: <https://www.mdpi.com/2077-1312/10/9/1318>. <https://dx.doi.org/10.3390/jmse10091318>.
- [6] S. Swenson, B. Argrow, E. Frew, S. Borenstein, J. Keeler, Development and deployment of air-launched drifters from small uas, *Sensors* 19 (2019) 2149.
- [7] L. F. Richardson, Atmospheric diffusion shown on a distance-neighbour graph, *Proceedings of the Royal Society of London. Series A, Containing Papers of a Mathematical and Physical Character* 110 (1926) 709–737.

- [8] D.-W. H. F. Sukkarieh S., Nebot E. M., A high integrity imu/gps navigation loop for autonomous land vehicle applications, *IEEE Transactions on Robotics and Automation* 15 (1999).
- [9] M. E. Paredes Quintanilla, S. Abdunabiev, M. Allegretti, A. Merlone, C. Musacchio, E. G. A. Pasero, D. Tordella, F. Canavero, Innovative mini ultralight radioprobes to track lagrangian turbulence fluctuations within warm clouds: Electronic design, *Sensors* 21 (2021). <https://dx.doi.org/10.3390/s21041351>.
- [10] U-Blox, ????
- [11] W. contributors, Nmea 0183 — Wikipedia, the free encyclopedia, 2022. URL: https://en.wikipedia.org/w/index.php?title=NMEA_0183&oldid=1116811683, [Online; accessed 8-Jan-2023].
- [12] T. C. Basso, G. Perotto, C. Musacchio, A. Merlone, A. Athanassiou, D. Tordella, Evaluation of mater bi and polylactic acid as materials for biodegradable innovative mini-radiosondes to track small scale fluctuations within clouds, *Materials Chemistry and Physics* 253 (2020) 123411. <https://dx.doi.org/10.1016/j.matchemphys.2020.123411>.
- [13] N. Yajima, T. Imamura, N. Izutsu, T. Abe, *Engineering Fundamentals of Balloons*, Springer New York, New York, NY, 2009, pp. 15–75. <https://dx.doi.org/10.1007/978-0-387-09727-5>.
- [14] S. Bertoldo, L. Carosso, E. Marchetta, M. Paredes, M. Allegretti, Feasibility analysis of a lora-based wsn using public transport, *Applied System Innovation* 1 (2018) 49.
- [15] S. Bertoldo, C. Lucianaz, M. Paredes, M. Allegretti, L. Carosso, P. Savi, Feasibility study of lora ad-hoc network in an urban noisy environment, in: *2018 18th Mediterranean Microwave Symposium (MMS)*, 2018, pp. 357–360. <https://dx.doi.org/10.1109/MMS.2018.8612027>.
- [16] M. Paredes, S. Bertoldo, L. Carosso, C. Lucianaz, E. Marchetta, M. Allegretti, P. Savi, Propagation measurements for a lora network in an urban environment, *Journal of Electromagnetic Waves and Applications* 33 (2019) 2022–2036. <https://dx.doi.org/10.1080/09205071.2019.1661287>.

- [17] ETSI, Short range devices (srd) operating in the frequency range 25 mhz to 1 000 mhz; part 2: Harmonised standard for access to radio spectrum for non specific radio equipment srds (25 mhz to 1 ghz)-part 2, 2022. URL: https://www.etsi.org/deliver/etsi_en/300200_300299/30022002/03.02.01_60/en_30022002v030201p.pdf, [Online; accessed 7-Jan-2023].
- [18] S. O. Madgwick, A. J. Harrison, R. Vaidyanathan, Estimation of IMU and MARG orientation using a gradient descent algorithm (2011) 1–7. <https://dx.doi.org/10.1109/ICORR.2011.5975346>.
- [19] R. E. Kalman, A New Approach to Linear Filtering and Prediction Problems, *Journal of Basic Engineering* 82 (1960) 35–45. <https://dx.doi.org/10.1115/1.3662552>.
- [20] D. Nath, M. Venkat Ratnam, A. K. Patra, B. V. Krishna Murthy, S. V. Bhaskar Rao, Turbulence characteristics over tropical station gadanki (13.5°n, 79.2°e) estimated using high-resolution gps radiosonde data, *Journal of Geophysical Research: Atmospheres* 115 (2010). URL: <https://agupubs.onlinelibrary.wiley.com/doi/abs/10.1029/2009JD012347>. <https://dx.doi.org/https://doi.org/10.1029/2009JD012347>. arXiv:<https://agupubs.onlinelibrary.wiley.com/doi/pdf/10.1029/2009JD012347>.
- [21] A. Jaiswal, D. V. Phanikumar, S. Bhattacharjee, M. Naja, Estimation of turbulence parameters using aries st radar and gps radiosonde measurements: First results from the central himalayan region, *Radio Science* 55 (2020) e2019RS006979. URL: <https://agupubs.onlinelibrary.wiley.com/doi/abs/10.1029/2019RS006979>. <https://dx.doi.org/https://doi.org/10.1029/2019RS006979>. arXiv:<https://agupubs.onlinelibrary.wiley.com/doi/pdf/10.1029/2019RS006979>.
- [22] BOSCH, Bme280 - combined humidity and pressure sensor, <https://www.bosch-sensortec.com/media/boschsensortec/downloads/datasheets/bst-bme280-ds002.pdf>, 2022. Rev. 1.23, [Online; accessed 16-Jan-2023].